Enhanced strength and temperature dependence of mechanical properties of Li at small scales and its implications for Li metal anodes

Chen Xu[a,1], Zeeshan Ahmad[b], Asghar Aryanfar[a], Venkatasubramanian Viswanathan[b,1], and Julia R. Greer[a]

[a]Division of Engineering and Applied Science, California Institute of Technology, Pasadena, CA 91125; and [b]Department of Mechanical Engineering, Carnegie Mellon University, Pittsburgh, PA 15213

Edited by Alexis T. Bell, University of California, Berkeley, CA, and approved November 28, 2016 (received for review September 22, 2016)

Most next-generation Li ion battery chemistries require a functioning lithium metal (Li) anode. However, its application in secondary batteries has been inhibited because of uncontrollable dendrite growth during cycling. Mechanical suppression of dendrite growth through solid polymer electrolytes (SPEs) or through robust separators has shown the most potential for alleviating this problem. Studies of the mechanical behavior of Li at any length scale and temperature are limited because of its extreme reactivity, which renders sample preparation, transfer, microstructure characterization, and mechanical testing extremely challenging. We conduct nanomechanical experiments in an in situ scanning electron microscope and show that micrometer-sized Li attains extremely high strengths of 105 MPa at room temperature and of 35 MPa at 90 °C. We demonstrate that single-crystalline Li exhibits a power-law size effect at the micrometer and submicrometer length scales, with the strengthening exponent of −0.68 at room temperature and of −1.00 at 90 °C. We also report the elastic and shear moduli as a function of crystallographic orientation gleaned from experiments and first-principles calculations, which show a high level of anisotropy up to the melting point, where the elastic and shear moduli vary by a factor of ∼4 between the stiffest and most compliant orientations. The emergence of such high strengths in small-scale Li and sensitivity of this metal's stiffness to crystallographic orientation help explain why the existing methods of dendrite suppression have been mainly unsuccessful and have significant implications for practical design of future-generation batteries.

dendrite | size effect | elastic anisotropy | dislocation | elevated temperature

Increased adoption of electric vehicles requires an improvement in the energy density of rechargeable Li ion batteries. Li metal anode is a common and necessary ingredient in commercialization pathways for next-generation Li ion batteries. In the near term, Li metal coupled with an advanced cathode could lead to a specific energy of 400 Wh/kg at the cell level, which represents 200% improvement over current state of the art (1). In the longer term, Li metal coupled with a S and O_2 cathode could lead to even higher specific energies of >500 Wh/kg. Despite over 40 y of research, overcoming the uncontrollable dendrite growth during cycling has remained an insurmountable obstacle for Li-based components (2). Among multiple attempted approaches to eliminate or even reduce the dendrite growth, mechanical suppression has emerged as one of the most promising routes. In their pioneering theoretical work, Monroe et al. (3) considered a solid polymer electrolyte (SPE) in contact with a Li metal electrode and performed a linear stability analysis of the deformation at the interface. They used linear elasticity to compute the stresses generated at the interface due to small deformations. They found that the dendrite growth decays with time if the shear modulus of the SPE is higher than about twice the shear modulus of Li through compressive forces. This led to enormous interest in demonstrating cells with polymer electrolytes, inorganic solid-state Li ion conductors, and ceramic thin films (2). Ferrese et al. (4) further demonstrated that the elastic modulus of the separator also affects dendrite growth because it causes the stress in the separator to build up to beyond the yield strength of Li, which causes the anode to plastically deform and flatten out. Applying external pressure higher than the yield strength of bulk polycrystalline Li in a direction perpendicular to the cell stack has also been shown to limit dendrite growth and prolong cycle life (5–7).

These approaches have had limited success, and many unsolved questions regarding mechanical suppression remain. For example, dendrites form and grow through the grain structure of Li garnet solid electrolytes even though their shear modulus is >50 GPa, a value predicted to be sufficiently high to suppress dendrite growth (8). Applying an external pressure above what is believed to be the yield strength of Li also does not fully eradicate dendrites, most likely because of the dearth of high-fidelity mechanical properties data for Li. Elastic modulus of polycrystalline Li has been reported to range from 1.9 to 7.9 GPa (9–12), and its yield strength, from 0.41 to 0.89 MPa (11, 12). Such a significant variation in both has been attributed to the differences in sample preparation methods, that is, melting and annealing conditions, reactivity with atmosphere, and experimental error. A key reason for the lack of solutions to overcome the Li dendrite growth challenge may be that the mechanical properties of Li at small scales are expected to drastically differ from those in its bulk form; most single-crystalline metals at the micrometer and submicrometer scales have been shown to be up to an order of magnitude stronger compared with their bulk form (13). During charging, crystalline Li whiskers with diameters on

Significance

Li metal anodes play a crucial part in next-generation Li ion and "beyond-Li ion" batteries. The issue of dendrites remains a major hurdle, and mechanical suppression through the use of solid electrolytes proves to be a promising solution. However, a lack of knowledge of mechanical properties of lithium metal at the micrometer scale limits our understanding of the mechanical interactions at the electrolyte/electrode interface. In this work, we report results on the mechanical properties of Li, specifically that Li exhibits a strong size effect at room and elevated temperature. First-principle calculations show a high level of elastic anisotropy. Based on the results, we present rational guidelines for anode/electrolyte selection and operating condition that will lead to better cycling performance.

Author contributions: C.X., Z.A., V.V., and J.R.G. designed research; C.X. and Z.A. performed research; A.A. contributed new reagents/analytic tools; C.X., Z.A., V.V., and J.R.G. analyzed data; and C.X., Z.A., V.V., and J.R.G. wrote the paper.

The authors declare no conflict of interest.

This article is a PNAS Direct Submission.

[1]To whom correspondence may be addressed. Email: chenxu@caltech.edu or venkvis@cmu.edu.

This article contains supporting information online at www.pnas.org/lookup/suppl/doi:10.1073/pnas.1615733114/-/DCSupplemental.

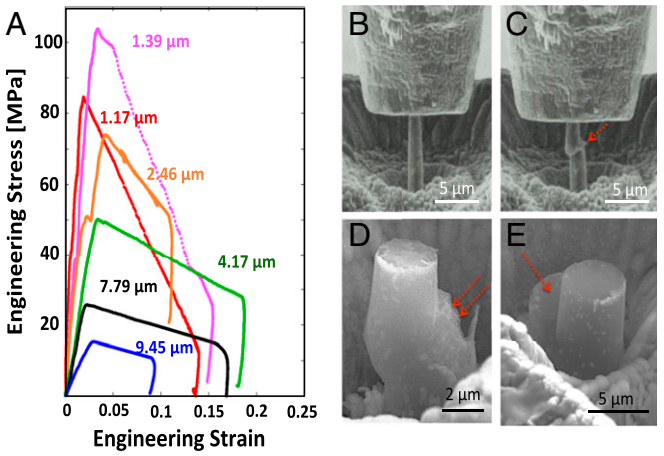

Fig. 1. Room temperature uniaxial compression experiments. (*A*) Engineering stress–strain data for Li pillars with different diameters. (*B* and *C*) Snapshots of in situ compression of a representative 1-μm-diameter Li pillar. (*D* and *E*) Compressed 4-μm-diameter Li pillars. Arrows point to slip offsets, likely along a <111> direction.

the order of a few hundred nanometers have been observed to nucleate on the anode surfaces (14), growing into dendrites up to several millimeters long. The size-independent properties, such as the elastic and shear moduli, are generally functions of crystallographic orientation, and are particularly sensitive to it in Li, whose anisotropy factor is 8.52 at room temperature (15). The mechanical properties of Li at high temperatures are also largely unknown. Current SPEs require an operating temperature of 333–363 K (60–90 °C) to achieve the desired ionic conductivity (10^{-3} S/cm) and strong adhesion to the electrodes. Li's low melting temperature of 453 K (180 °C) suggests that even a modest temperature elevation will likely have a dramatic effect on its mechanical properties.

In this work, we aim to fill the gaps in the existing, severely incomplete understanding of the mechanical properties of Li. We performed uniaxial compression experiments on single-crystalline Li pillars with diameters of 980 nm to 9.45 μm at 298 and 363 K in an in situ nanomechanical instrument inside of an SEM chamber. We observed a pronounced size effect in yield strength at room temperature, with the power law exponent of strength vs. pillar diameter of −0.68, a value that is higher than those reported for most body-centered cubic metals (13, 16). This size effect becomes more pronounced at 363 K, where the exponent decreases to −1.00. We further observed a dramatic decrease in yield strength across all pillar sizes at 363 K compared with that at room temperature, by a factor of ∼3.5. To address the mechanical properties in the elastic regime, density functional theory (DFT) calculations were performed to determine the elastic constants as a function of temperature from 78 to 440 K and found them to be in good agreement with experimental values, where applicable (78–300 K) (17, 18). Size-independent properties such as the elastic and shear moduli were calculated as a function of crystal orientation and temperature. We discuss the impact of the discovered size effect and of elastic anisotropy on Li dendrite growth in the framework of nanocrystalline plasticity and provide insights into the shortcomings of the existing dendrite suppression methods, as well as into the potential pathways to use these findings in designing safer and more efficient energy storage systems.

Fig. 1*A* shows representative engineering stress vs. engineering strain data for room temperature compression of Li micropillars with different diameters. All curves exhibit an initial elastic loading segment followed by plastic flow, ending in catastrophic failure at a strain of 2–3%. The initial loading slope corresponds to the stiffness of each sample; the differences in these slopes are caused by the different crystallographic orientations of the samples, as well as possible effects of slight initial misalignment during the experiments (19). We observed a pronounced increase in the yield and flow stresses as the pillar diameter was decreased. The yield strength, defined as the stress at which the first significant strain burst occurs, increases from 15 to 105 MPa as the pillar diameter decreases from 9.45 to 1.39 μm. Fig. 1 *B* and *C* shows snapshots of a 1-μm pillar during compression, where the pillar sheared off via a single slip offset. Fig. 1 *D* and *E* shows SEM images of some representative Li pillars deformed at room temperature, with characteristic sharp and localized slip traces.

We performed another series of microcompression experiments at 363 K. Fig. 2 *A* and *B* shows the mechanical response of Li pillars at 363 K compared with room temperature experiments. These plots reveal that the yield strength of ∼1-μm-diameter samples at 363 K is around 35 MPa, compared with ∼95 MPa at 298 K; and for 8.5-μm diameters, the yield strength is 5 MPa at 363 K compared with 16 MPa at 298 K. A modest decrease in yield strength during higher temperature deformation has been reported for other bcc metals (20–22); a factor of 3 decrease in yield strength of Li at only 65 K higher temperature discovered in this work has not been observed before. Tariq et al. (12) reported the ultimate tensile strength of bulk polycrystalline Li deformed at a strain rate 2×10^{-3} s^{-1} at room temperature to be 0.89 MPa, and 0.46 MPa at 75 °C. Fig. 2 *C* and *D* shows SEM images taken during in situ compression of an 8.5-μm-diameter pillar and reveals that, unlike in room temperature experiments, this sample experiences barreling with no visible crystallographic slip offsets.

Fig. 3*A* shows the plot of critical resolved shear stress (CRSS) at 2% strain as a function of pillar diameter on a log–log scale. We chose the most common slip system in bcc metals, {100}<111> (23), to calculate CRSS for all experiments by multiplying the axial flow stress at 2% strain by the maximum Schmidt factor allowed for the slip system. The crystallographic orientation of

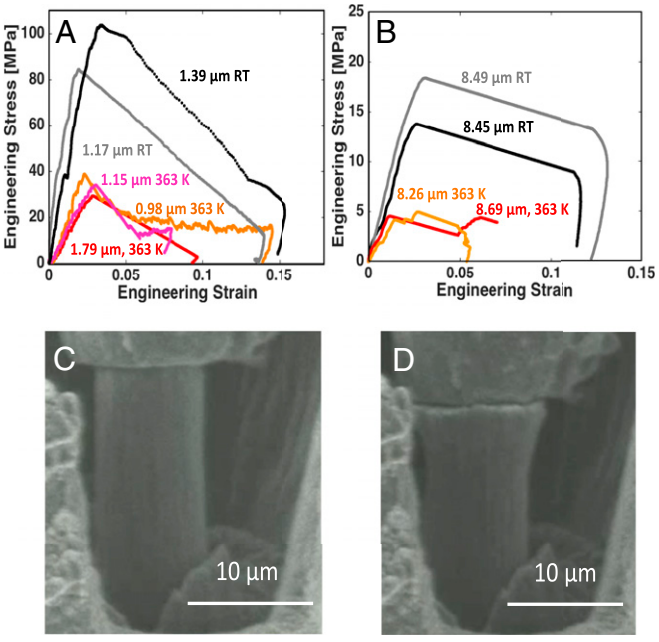

Fig. 2. Uniaxial compression at 363 K. Engineering stress vs. engineering strain for compression of Li pillars with diameters of (*A*) ∼1 μm and (*B*) ∼8 μm at room temperature (RT) and 363 K. (*C* and *D*) Snapshots of in situ compression of a 9-μm-diameter Li pillar at 363 K, which shows barreling and no crystallographic offsets.

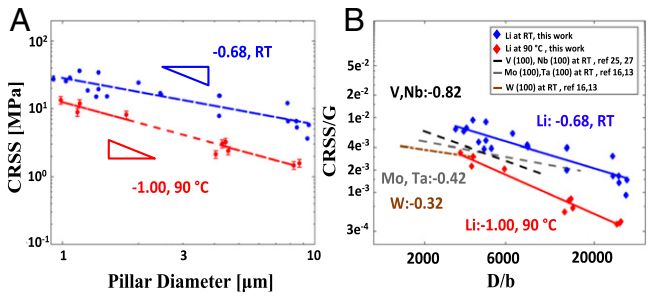

Fig. 3. Size effect in Li at room temperature (RT) and 363 K compared with other BCC metals. (*A*) CRSS vs. pillar diameter for RT and 363 K experiments. Error bars are plotted for those data points where pillars bent after catastrophic failure, causing the unloading data to no longer reflect the stiffness. In those cases, the Schmidt factor may range from 0.500 to 0.272, and the error bars represent 1 SD. (*B*) CRSS normalized by the bulk shear modulus vs. pillar diameter normalized by the Burgers vector for different single-crystalline bcc metals. The values for the slopes are of the CRSS vs. *D*, not the normalized values.

each pillar was estimated either directly from electron backscatter diffraction (EBSD) map or from the unloading data when EBSD mapping was unavailable (details given in *Supporting Information*). We found the power law slope for size-dependent strengthening of Li at room temperature to be −0.68 and −1.00 at 363 K. Fig. 4*B* shows the CRSS normalized by the shear modulus, $G(3)$, as a function of the pillar diameter, D, normalized by the Burgers vector, b (24), for Li and several other BCC metals deformed at room temperature. It shows that at room temperature, Li has the highest relative strength among all metals in this size range. Additionally, the size effect slope for Li deformed at 363 K is higher than virtually all other size effect slopes reported for single-crystalline BCC metals (13).

In addition to strength, the elastic properties of Li, such as the moduli, which are size independent, are also expected to affect Li dendrite growth (3). In a single crystal, the elastic properties such as the shear modulus, G, elastic modulus, E, and Poisson's ratio, v vary with crystallographic orientation. Li has a very high anisotropy factor of 8.52, defined as $A = 2C_{44}/(C_{11} - C_{12})$, where C_{11}, C_{21}, and C_{44} are elastic constants (17, 18). This implies that the mechanical properties of each Li grain vary significantly with orientation, which leads to a broad range in shear and elastic moduli and different propensity for dendrite formation and growth. Experimental values of elastic constants as a function of temperature exist only in the range of 78–300 K (17, 18). We used DFT to calculate the elastic constants of Li between 78 and 440 K. Fig. 4*A* shows C_{11}, C_{12}, and C_{44}, plotted as a function of temperature along with the experimental data from Slotwinski and Trivisonno (78–300 K) (18). This plot reveals that the predicted values agree with the experimental data in the 78–300 K range within ∼5–10%. Using both sets of elastic constants as input, we calculated E, G, and the bulk modulus B, and plotted them as a function of temperature in Fig. 4 *B* and *D*. Details of the calculation are given in *Supporting Information*. The plot in Fig. 4*B* shows an excellent agreement in B between DFT and those calculated using experimental elastic constants, with an average variance of 2.51% within the entire temperature range. Fig. 4*C* depicts the temperature dependence of $E_{<111>}$ (stiffest orientation) and $E_{<100>}$ (most compliant orientation) and shows that, at 300 K, DFT predicts $E_{<111>}$ to be 21.1 GPa and $E_{<100>}$ to be 4.79 GPa; and calculation based on experimental elastic constants (18) reveal $E_{<111>}$ to be 21.2 GPa and $E_{<100>}$ to be 3.00 GPa. Fig. 4*D* show the temperature dependence of $G_{<100>}$ and $G_{<111>}$ and reveals that, at room temperature, the DFT predicts 8.68 GPa along <100>, whereas calculations from experimental data yield 8.78 GPa; respective values for <111> are 2.28 and 1.46 GPa. An interesting observation is that, in shear, the stiffest orientation is <100>, and the most compliant is <111>, which is diametrically opposite to axial loading, with the stiffest orientation being <111> and most compliant <100>. At 440 K, DFT predicts a moderate decrease of 1.49% and 0.85% for $G_{<100>}$ and $G_{<111>}$, respectively. Fig. 4 *E* and *F* shows spherical plots of the directional dependence of elastic and shear modulus, respectively.

The postmortem localized deformation via crystallographic slip exhibited by Li at room temperature (Fig. 1 *B* and *E*) is similar to those reported for Nb (16, 25) and V (19) nanopillars deformed at room temperature; the deformation of Mo and W nanopillars is characterized by uniform deformation with wavy slip traces (16, 21, 26). A common trait shared by Nb and V is a

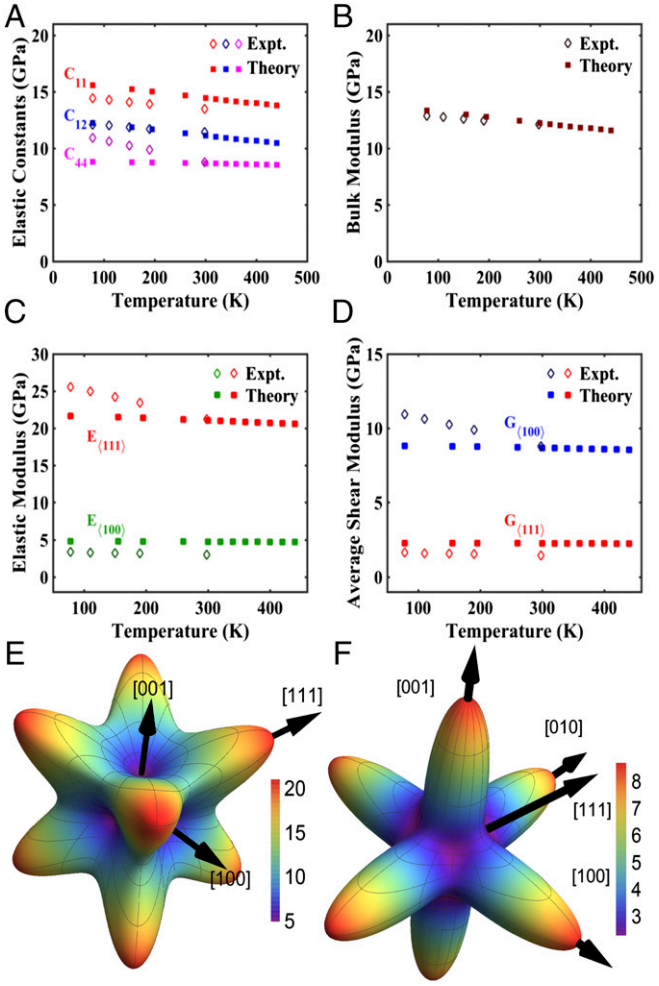

Fig. 4. Elastic properties of single-crystalline Li at different temperatures and in different crystallographic orientations. (*A*) Elastic constants C_{11}, C_{12}, and C_{44} as a function of temperature. Solid squares (■) represent DFT calculations (this work), and diamonds (♢) represent experimental values taken from Slotwinski and Trivisonno (18). (*B*) Bulk modulus vs. temperature. Solid squares (■) represent DFT calculations, whereas diamonds (♢) represent values calculated using data from Slotwinski and Trivisonno (18). (*C*) Maximum elastic modulus ($E_{<111>}$) and minimum elastic modulus ($E_{<100>}$) as a function of temperature as calculated by DFT and gleaned from experiments. (*D*) Maximum average shear modulus ($G_{<100>}$) and minimum average shear modulus ($G_{<111>}$) as a function of temperature as calculated by DFT and gleaned from experiments. (*E*) Directional dependence of the elastic modulus (in gigapascals) of Li, using elastic constants obtained via DFT calculations. (*F*) Directional dependence of the shear modulus (in gigapascals) of Li, using elastic constants obtained via DFT calculations.

low critical temperature (T_c), defined as the temperature at which screw and edge dislocations have similar mobility, and the effects of intrinsic lattice resistance become negligible (16, 25). A lack of closest-packed planes in bcc metals and the nonplanarity of screw dislocation cores leads to their motion via cross-slip rather than glide-only and to their experiencing a higher effective Peierls' barrier compared with that of the edge dislocations. At higher temperatures, the thermally activated screw dislocations are able to move more easily through the potential energy landscape until T_c, when their mobility becomes virtually equivalent to that of edge dislocations. At that point, it becomes possible to initiate an avalanche of dislocations gliding on a single slip plane, resulting in localized slip offsets, a common characteristic of deformation in fcc pillars (13). T_c for Nb is 350 K and that for V is 380 K, which are low enough that compression at room temperature produces fcc-like deformation (27), whereas Mo and W have T_c values of 480 and 800 K, which leads to the waviness in the slip patterns during room temperature deformation (16). It is not surprising that Li would exhibit similar fcc-like deformation behavior as Nb and V, because although no report exists on the T_c of Li, it is likely to be lower than its melting temperature of 453 K. In our experiments at 363 K, the postmortem images show a transition from localized to homogeneous deformation, which is likely related to the low melting point of Li and the high homologous temperature of the experiments, $T_{test}/T_{melting}$, which is 0.65 at 298 K, and 0.8 at 363 K. At high homologous temperatures, the dislocation movement is no longer confined to slip planes with the largest resolved shear stress because thermally activated processes like cross-slip and dislocation climb become possible (28). This also explains the observed decrease in yield strength (Fig. 2 *A* and *B*) compared with room temperature deformation.

The large size effect at room temperature may be explained by one of two mechanisms: (*i*) dislocation multiplication-driven plasticity (29, 30), where the entanglement of the dislocation segments contribute to increased flow stress in a manner similar to forest hardening in bulk crystals; or (*ii*) dislocation nucleation-governed plasticity, commonly observed in the deformation of small-scale single-crystalline metals, which is accommodated by dislocation nucleation—most likely at the existing single-arm sources and/or at the surfaces—which occurs at ever higher flow stresses (27). At 363 K, the enhancement in size effect might be caused by the increased mobility of the screw dislocations, which causes the rate of dislocation annihilation to increase and to transition overall deformation to nucleation-driven plasticity sooner. This is consistent with the size effect plot in Fig. 3*B*, which shows that, at room temperature, the power law slope of −0.68 for Li is close to those of V (−0.79) and Nb (−0.93) (19), the two bcc metals exhibiting fcc-like deformation and size effect exponent. This plot also reveals that, relative to the shear modulus, Li is the strongest of all reported bcc metals within the studied size range; for example, at a pillar diameter of 1 μm (D/b = 3,300), the relative strength of Li is a factor of 1.7 higher than V and Nb, and a factor of 2.3 higher than W. At 363 K, the size effect slope becomes −1.00, whereas the normalized strength decreases by a factor of ∼3.5 compared with room temperature over the entire size range.

This size effect has important implications for dendrite formation and growth that may explain why applying an external pressure higher than what is believed to be the bulk yield strength of Li at room temperature, 0.41–0.89 MPa (4, 11), on a cell stack has not fully prevented dendrite formation (5–7). Our findings demonstrate that, during the initial stages of dendrite nucleation and growth, the yield strength of nanoscale dendrites exceeds that of the externally applied pressure, which is what allows them to grow. As the dendrites expand, their yield strength decreases to the point where it is balanced by the applied pressure, which drives them to deform plastically and promotes the in-plane growth of Li (5, 7), leading to a smoother surface at the top of the deposit. The high yield strength also causes an appreciable change in the kinetics of dendrite growth through the pressure term in the modified Butler–Volmer equation (3, 4). At higher temperatures, the dramatic decrease in yield strength may explain why dendrite suppression is more easily achieved (31).

Unlike the yield strength, the elastic properties have a weak dependence on temperature. Our DFT calculations of C_{11}, C_{12}, and C_{44} capture the expected asymptotic linear reduction with temperature, saturating at a finite value near the melting point, as often exhibited by other cubic crystals (32). It is encouraging that, although DFT calculations have sometimes been found to poorly predict C_{44} (33), our DFT prediction of C_{44} for room temperature value agrees well with experimental data (1.14% difference). Fig. 4 *C* and *D* shows that the large difference between the strongest and weakest crystal orientation persists throughout the entire studied temperature range. Our results indicate that, according to the linear stability analysis by Monroe and Newman (3), dendrites originating from the <100>-oriented grain in a typical polycrystalline (MTI Corporation; www.mtixtl.com/Li-Foil-30000mmL-35mmW-0.17mmTh.aspx) Li anode would require a separator with a shear modulus of at least 17.5 GPa to suppress them, whereas a much lower value of 2.92 GPa is sufficient for the <111> orientation. This holds as long as no dendrite growth occurs through pores or grain boundaries, which can be achieved by using dense electrolyte preparation methods like pressure-assisted sintering (8).

Our results provide insights into the mechanical properties of Li as a function of sample dimensions, temperature, and crystallographic orientation, and have significant implications for Li dendrite growth, as well as provide guidelines for their suppression. The discovered yield strength of 1-μm-sized Li of 105 MPa at room temperature represents a two-orders of magnitude increase over what is believed to be the bulk strength of Li, 0.41–0.89 MPa (4, 11), and exposes serious shortcomings of the current mechanical methods of dendrite suppression. The observed threefold decrease in yield strength at 363 K (operating temperature of many SPEs) is substantial compared with the marginal decrease in shear modulus, which indicates that, at high temperatures, dendrite suppression via inducing plastic deformation will be much more effective than finding SPEs with higher shear moduli. The high elastic anisotropy warrants the move to beyond the simple isotropic treatment of most existing theoretical efforts. More attention needs to be paid to the variation of elastic and shear moduli in the polycrystalline anode when designing SPEs with high shear modulus or when fabricating Li anodes rich in compliant orientations. Based on our experimental data and theoretical analysis, a Li metal anode operating under elevated temperature and/or having an interfacial orientation with a low shear modulus, for example <111>, in contact with a solid electrolyte with high elastic modulus will be less prone to dendrite formation. The rational design guidelines and the high-fidelity data provided will rapidly accelerate the development of a reversible Li metal anode, paving the way for higher energy density Li ion batteries or "beyond-Li ion" chemistries such as Li–S or Li–O_2.

Materials and Methods

Sample Preparation. Li granules (Sigma-Aldrich) were melted on a hot plate in an argon glovebox at 180 °C, and then cooled down to room temperature over 4 h. The sample was then cut with a surgical blade to reveal a shiny metallic surface, from which we fabricated the nanocompression and microcompression samples. This parent Li sample was placed into an airtight transfer module (Vacushut; Agar Scientific) and carried from the glovebox to the SEM without exposure to the atmosphere. Ar was used to vent the SEM. Once inside the SEM chamber, the lid of the Vacushut self-opened as the chamber was pumped down to vacuum. We fabricated cylindrical pillars with diameters ranging from 980 nm to 9.45 μm in a focused ion beam (FIB) (Versa DualBeam; FEI); the aspect ratio, height/diameter, was maintained

between 3:1 and 5:1. The tops of the pillars were polished in the FIB to minimize surface roughness.

Mechanical Characterization. After fabrication, the sample was carried in the Vacushut from the FIB to the in situ nanomechanical instrument, SEMentor (InSEM; Nanomechanics and FEI) (Fig. S1). SEMentor allows us to simultaneously capture the real-time deformation video and to collect mechanical data during the experiments. Samples were compressed using a custom-made diamond flat punch tip with a diameter of ~12 μm, and all experiments were conducted under a constant nominal strain rate of 5×10^{-3} s^{-1}. Engineering stresses and strains were calculated by dividing the applied force and displacement by the initial cross-sectional area and pillar height, respectively. The initial cross-sectional area was calculated based on the SEM images, using the pillar diameter measured at halfway along the pillar height. We accounted for the compliance of the substrate using Sneddon's correction (34). SEMentor is equipped with a heating module located directly underneath the sample mount, which allows us to heat the sample up to 200 °C. We used a thermocouple located within the sample mount and connected to a PID temperature controller (Lake Shore Cryotronics) to carefully maintain the sample at the set temperature. We found that the sample stabilized at 363 K (90 °C) after 3 h. To avoid significant thermal drift, that is, recorded displacement caused by thermal expansion of the tip/sample and possible temperature fluctuations during compression, the tip was placed in contact with the Li substrate for at least 3 h to equilibrate the temperature before each test. We recorded typical thermal drift after each test to be <5 nm/s, which we used to correct the stress–strain data.

DFT Calculations. We use the quasiharmonic approximation to account for the free-energy contribution from lattice vibrations (35). Calculations were performed using a real-space projector augmented wave (PAW) (36) method as implemented in GPAW (37) within the generalized gradient approximation (38). A real-space grid spacing of 0.18 Å and Monkhorst Pack (39) scheme for *k*-points consisting of 3,456 *k*-points per reciprocal atom or higher was used. All calculations were converged to the energy of <0.1 meV and a force of <0.01 eV/Å. The phonon vibrational frequencies and the density of states were calculated using the small displacement method (40) as implemented in atomic simulation environment (41). A 32-atom supercell of lithium was used for all phonon calculations. The lattice constant at each temperature was calculated by free-energy minimization and the vibrational contribution to free energy was calculated at each of the temperatures using a method described in *Supporting Information*.

ACKNOWLEDGMENTS. We thank Dr. Chi Ma for EBSD assistance and useful discussions. We gratefully acknowledge the financial support of the US Department of Energy through J.R.G.'s Early Career Grant DE-SC0006599. This work was supported by National Science Foundation CAREER Award CBET-1554273 (to V.V.).

1. Christensen J, et al. (2012) A critical review of Li/air batteries. *J Electrochem Soc* 159(2): R1–R30.
2. Xu W, et al. (2014) Lithium metal anodes for rechargeable batteries. *Energy Environ Sci* 7(2):513–537.
3. Monroe C, Newman J (2005) The impact of elastic deformation on deposition kinetics at lithium/polymer interfaces. *J Electrochem Soc* 152(2):A396–A404.
4. Ferrese A, Newman J (2014) Mechanical deformation of a lithium-metal anode due to a very stiff separator. *J Electrochem Soc* 161(9):A1350–A1359.
5. Wilkinson DP, Blom H, Brandt K, Wainwright D (1991) Effects of physical constraints on Li cyclability. *J Power Sources* 36(4):517–527.
6. Hirai T (1994) Influence of electrolyte on lithium cycling efficiency with pressurized electrode stack. *J Electrochem Soc* 141(3):611–614.
7. Gireaud L, Grugeon S, Laruelle S, Yrieix B, Tarascon J-M (2006) Lithium metal stripping/plating mechanisms studies: A metallurgical approach. *Electrochem Commun* 8(10):1639–1649.
8. Ren Y, Shen Y, Lin Y, Nan C-W (2015) Direct observation of lithium dendrites inside garnet-type lithium-ion solid electrolyte. *Electrochem Commun* 57:27–30.
9. Bridgman PW (1922) The effect of tension on the electrical resistance of certain abnormal metals. *Proc Am Acad Arts Sci* 57(3):41–66.
10. Robertson W, Montgomery D (1960) Elastic modulus of isotopically-concentrated lithium. *Phys Rev* 117(2):440–442.
11. Schultz RP (2002) *Lithium: Measurement of Young's Modulus and Yield Strength* (Fermi National Accelerator Laboratory, Batavia, IL), Technical Report FERMILAB-TM-2191.
12. Tariq S, et al. (2003) Li material testing—Fermilab antiproton source lithium collection lens. *Proceedings of the 2003 Bipolar/BiCMOS Circuits and Technology Meeting* (IEEE, Piscataway, NJ), IEEE catalog no. 03CH37440, pp 1452–1454.
13. Greer JR, De Hosson JTM (2011) Plasticity in small-sized metallic systems: Intrinsic versus extrinsic size effect. *Prog Mater Sci* 56(6):654–724.
14. Liu XH, et al. (2011) Lithium fiber growth on the anode in a nanowire lithium ion battery during charging. *Appl Phys Lett* 98(18):183107.
15. Simmons G, Wang H (1971) *Single Crystal Elastic Constants and Calculated Aggregate Properties a Handbook* (MIT, Cambridge, MA).
16. Schneider AS, et al. (2009) Correlation between critical temperature and strength of small-scale bcc pillars. *Phys Rev Lett* 103(10):105501.
17. Trivisonno J, Smith CS (1961) Elastic constants of lithium-magnesium alloys. *Acta Metall* 9(12):1064–1071.
18. Slotwinski T, Trivisonno J (1969) Temperature dependence of the elastic constants of single crystal lithium. *J Phys Chem Solids* 30(5):1276–1278.
19. Han SM, Bozorg-Grayeli T, Groves JR, Nix WD (2010) Size effects on strength and plasticity of vanadium nanopillars. *Scr Mater* 63(12):1153–1156.
20. Schneider AS, Frick CP, Arzt E, Clegg WJ, Korte S (2013) Influence of test temperature on the size effect in molybdenum small-scale compression pillars. *Philos Mag Lett* 93(6):331–338.
21. Torrents Abad O, Wheeler JM, Michler J, Schneider AS, Arzt E (2016) Temperature-dependent size effects on the strength of Ta and W micropillars. *Acta Mater* 103: 483–494.
22. Lee S-W, Cheng Y, Ryu I, Greer JR (2014) Cold-temperature deformation of nano-sized tungsten and niobium as revealed by in-situ nano-mechanical experiments. *Sci China Technol Sci* 57(4):652–662.
23. Weinberger CR, Boyce BL, Battaile CC (2013) Slip planes in bcc transition metals. *Int Mater Rev* 58(5):296–314.
24. Kellington SH, et al. (1969) The lattice parameters of some alloys of lithium. *J Phys D Appl Phys* 2(8):1162.
25. Kim J-Y, Jang D, Greer JR (2010) Tensile and compressive behavior of tungsten, molybdenum, tantalum and niobium at the nanoscale. *Acta Mater* 58(7):2355–2363.
26. Kim J-Y, Jang D, Greer JR (2012) Crystallographic orientation and size dependence of tension–compression asymmetry in molybdenum nano-pillars. *Int J Plast* 28(1):46–52.
27. Min Han S, et al. (2013) Critical-temperature/Peierls-stress dependent size effects in body centered cubic nanopillars. *Appl Phys Lett* 102(4):41910.
28. Lee G, Kim J-Y, Burek MJ, Greer JR, Tsui TY (2011) Plastic deformation of indium nanostructures. *Mater Sci Eng A* 528(19–20):6112–6120.
29. Greer JR, Weinberger CR, Cai W (2008) Comparing the strength of f.c.c. and b.c.c. submicrometer pillars: Compression experiments and dislocation dynamics simulations. *Mater Sci Eng A* 493(1-2):21–25.
30. Weinberger CR, Cai W (2008) Surface-controlled dislocation multiplication in metal micropillars. *Proc Natl Acad Sci USA* 105(38):14304–14307.
31. Khurana R, Schaefer JL, Archer LA, Coates GW (2014) Suppression of lithium dendrite growth using cross-linked polyethylene/poly(ethylene oxide) electrolytes: A new approach for practical lithium-metal polymer batteries. *J Am Chem Soc* 136(20): 7395–7402.
32. Collard SM, McLellan RB (1991) High-temperature elastic constants of gold single-crystals. *Acta Metall Mater* 39(12):3143–3151.
33. Weinberger CR, Tucker GJ, Foiles SM (2013) Peierls potential of screw dislocations in bcc transition metals: Predictions from density functional theory. *Phys Rev B* 87(5): 54114.
34. Greer JR, Oliver WC, Nix WD (2005) Size dependence of mechanical properties of gold at the micron scale in the absence of strain gradients. *Acta Mater* 53(6):1821–1830.
35. Ackland GJ, Huang X, Rabe KM (2003) First-principles thermodynamics of transition metals: W, NiAl, and PdTi. *Phys Rev B* 68(21):214104.
36. Blöchl PE (1994) Projector augmented-wave method. *Phys Rev B Condens Matter* 50(24):17953–17979.
37. Mortensen JJ, Hansen LB, Jacobsen KW (2005) Real-space grid implementation of the projector augmented wave method. *Phys Rev B* 71(3):35109.
38. Perdew JP, Burke K, Ernzerhof M (1996) Generalized gradient approximation made simple. *Phys Rev Lett* 77(18):3865–3868.
39. Monkhorst HJ, Pack JD (1976) Special points for Brillouin-zone integrations. *Phys Rev B* 13(12):5188–5192.
40. Alfè D (2009) PHON: A program to calculate phonons using the small displacement method. *Comput Phys Commun* 180(12):2622–2633.
41. Bahn SR, Jacobsen KW (2002) An object-oriented scripting interface to a legacy electronic structure code. *Comput Sci Eng* 4(3):56–66.
42. Nash HC, Smith CS (1959) Single-crystal elastic constants of lithium. *J Phys Chem Solids* 9(2):113–118.
43. Aitken ZH, Fan H, El-Awady JA, Greer JR (2015) The effect of size, orientation and alloying on the deformation of AZ31 nanopillars. *J Mech Phys Solids* 76:208–223.
44. Bower AF (2009) *Applied Mechanics of Solids* (CRC, Boca Raton, FL).
45. Greer JR, Nix WD (2006) Nanoscale gold pillars strengthened through dislocation starvation. *Phys Rev B* 73(24):245410.
46. Turley J, Sines G (1971) The anisotropy of Young's modulus, shear modulus and Poisson's ratio in cubic materials. *J Phys D Appl Phys* 4(2):264.
47. Mehl MJ, Klein BM, Papaconstantopoulos DA (1994) First-principles calculation of elastic properties. *Intermetallic Compounds, Vol 1, Principles*, eds Westbrook JH, Fleischer RL (Wiley, Chichester, UK), pp 195–210.
48. Pham HH, et al. (2011) Finite-temperature elasticity of fcc Al: Atomistic simulations and ultrasonic measurements. *Phys Rev B* 84(6):64101.
49. Birch F (1947) Finite elastic strain of cubic crystals. *Phys Rev* 71(11):809–824.
50. Quong AA, Liu AY (1997) First-principles calculations of the thermal expansion of metals. *Phys Rev B* 56(13):7767–7770.